Melting behavior of water in cylindrical pores: carbon nanotubes and silica glasses

M. Sliwinska-Bartkowiak,*[a] M. Jazdzewska,[a] L. L. Huang[b] and K. E. Gubbins*[b]

Received 15th May 2008, Accepted 27th June 2008
First published as an Advance Article on the web 16th July 2008
DOI: 10.1039/b808246d

We report a study of the effects of confinement in multi-walled carbon nanotubes and mesoporous silica glasses (SBA-15) on the solid structure and melting of both H_2O and D_2O ice, using differential scanning calorimetry, dielectric relaxation spectroscopy, and neutron diffraction. Multi-walled nanotubes of 2.4, 3.9 and 10 nm are studied, and the SBA-15 studied has pores of mean diameter 3.9 nm; temperatures ranging from approximately 110 to 290 K were studied. We find that the melting point is depressed relative to the bulk water for all systems studied, with the depression being greater in the case of the silica mesopores. These results are shown to be consistent with molecular simulation studies of freezing in silica and carbon materials. The neutron diffraction data show that the cubic phase of ice is stabilized by the confinement in carbon nanotubes, as well as in silica mesopores, and persists up to temperatures of about 240 K, above which there is a transition to the hexagonal ice structure.

Introduction

Water confined in a nanoscale environment exhibits unique properties, and has been the subject of much attention. Of particular interest have been the effects of phase transitions on water in confined systems,[1–5] structure of water and ice in nanopores[6–9] and dynamical properties of water in one-dimensional pores.[9–12]

The structure of water in nanopores has not been as fully explored as that of bulk water. There are at least 13 ice polymorphs of bulk water. The phase diagram of ice exhibits many different crystal forms depending on local molecular correlations that influence the ordered arrangement of hydrogen-bonded configurations. In addition to these stable structures there are also a number of metastable states, which depend on less ordered hydrogen-bond arrangements. The inter-relation of these various structures has been a source of difficulties in establishing the complex behavior of the solid state of confined water.

I. Methods

In this paper we report experimental studies of the melting transition for D_2O and H_2O water confined in opened multiwall carbon nanotubes (MWNT) having average inner diameters of 2.4, 3.9 and 10 nm, produced and characterized by NANOCYL Co., Belgium. Differential scanning calorimetry (DSC) and dielectric relaxation spectroscopy (DRS) were used to determine the melting temperature of confined H_2O and D_2O water. The structure of the confined ice was determined by neutron diffraction (ND). In the neutron scattering experiments we used D_2O water to avoid the complications of incoherent scattering and inelasticity corrections that arise in the case of H_2O. The MWNT samples were heated to about 400 K and kept under vacuum (10^{-3} Tr) for a few days to remove the air prior to and during the introduction of the water. In our experiments we have used D_2O (100% deuterium) from Sigma. The H_2O water samples were distilled and demineralised using a Millipore apparatus. The conductivity of the purified water was on the order of $10^{-6}\ \Omega^{-1}\ m^{-1}$.

Differential scanning calorimetry

A Netzsch DSC204 Phoenix differential scanning calorimeter (DSC) was used to determine the melting temperatures of the bulk and confined water by measuring the heat released in the melting of D_2O water. Temperature scanning rates of 2–5 K min^{-1} were used in the experiments. The melting temperatures were determined from the position of the peaks of the heat flow signals during the warming process and were reproducible to within 0.5 K.

Dielectric relaxation spectroscopy

The melting of D_2O confined in MWNTs has also been investigated by dielectric relaxation spectroscopy (DRS), as described elsewhere.[13–17] The dielectric constant is a natural choice of order parameter to study melting of dipolar liquids, because of the large change in the orientational polarizability between the solid and the liquid phases.[17,18] The complex electric permittivity, $\kappa = \kappa' + i\kappa''$ where $\kappa' = C/C_0$ is the real, and $\kappa'' = \tan(\delta)/\kappa'$ is the complex, part of the permittivity, was measured in the frequency interval 10^6–10 MHz at different temperatures using a Solartron 1260 impedance gain analyzer, with a parallel plate capacitor made of stainless steel. Here C is the electric capacitance, C_0 is the capacitance in the absence of the dielectric medium, and δ is the angle by which the current leads the voltage due to dielectric loss. In order to reduce the

---

[a] *Institute of Physics, Adam Mickiewicz University, Umultowska 85, 61-614 Poznan, Poland. E-mail: msb@amu.edu.pl*
[b] *Department of Chemical and Biomolecular Engineering, North Carolina State University, 911 Partners' Way, Raleigh, NC 27695-7905, USA. E-mail: keg@ncsu.edu*

high conductivity of the sample, which was placed between the capacitor plates as a suspension of water-filled MWNTs in pure liquids, the electrodes were covered with a thin layer of Teflon. From the directly measured capacitance, C, and the tangent loss $\tan(\delta)$, the values of κ' and κ'' were calculated for the known sample geometry. The temperature was controlled to an accuracy of 0.1 K using a platinum resistor Pt (100) as a sensor and a K30 Modinegen external cryostat coupled with a N-180 ultra-cryostat.

For an isolated dipole rotating under an oscillating field in a viscous medium, the Debye dispersion relation is derived in terms of classical mechanics

$$\kappa^* = \kappa_\infty' + (\kappa_s' + \kappa')/(1 + i\omega\tau) \qquad (1)$$

Where ω is the frequency of the potential applied, and τ is the orientational relaxation time of a dipolar molecule. The subscript s refers to the static permittivity, *i.e.* the permittivity in the low frequency limit, when the dipoles have enough time to be in phase with the applied field. The subscript ∞ refers to the high frequency limit of the permittivity, and is a measure of the induced component of the permittivity. The dielectric relaxation time was calculated by fitting the dispersion spectrum of the complex permittivity near resonance to the Debye model of orientational relaxation.

Neutron diffraction

Neutron diffraction experiments have been performed using the DN-2 diffractometer at the IBR-2 pulsed reactor in the Frank Laboratory of Neutron Physics in Dubna, Russia, using an incident wavelength of 2 Å. The DN-2 is a multipurpose time-of-flight diffractometer with an d_{hkl} interplanar spacing range from 0.6 to 20 Å (average resolution $\Delta d/d \sim 2\%$), and neutron flux at the sample of $\sim 10^7$ n cm^{-2} s^{-1}). The scattering angle, $2\theta \sim 162^\circ$, was fixed. The sample in a vanadium container (with diameter 5 mm, height 15 mm) was cooled to about 100 K and then warmed to 300 K. Structure refinement was carried out using the FullProf program based on the multi-phase Rietveld analysis method.[19–21] The Rietveld refinement is a structure refinement method which does not use integrated neutron powder intensities, single or overlapping, but employs directly the profile intensities obtained from step-scanning measurements of the powder diagram. Nuclear, as well as magnetic structure can be refined, with the assumption of the Gaussian peak shape for each Bragg peak.

II. Experimental results

Water in carbon nanotubes

The melting temperatures of water confined in MWNTs with inner diameters of 2.4, 3.9 and 10 nm were determined using both DSC and DRS. The measurements were performed for both H_2O and D_2O water, as D_2O is used in the neutron scattering experiments. Results of the measurements of C for bulk H_2O and D_2O water during the heating process as a function of T and at a frequency of 0.6 MHz are shown in Fig. 1. There is a sharp increase in C at $T = 273.1$ K for H_2O and at 276.9 K for D_2O water, the melting points of the pure substances, due to the contribution to the orientational polarization[14,15] in the liquid state from the permanent dipoles. In the frequency interval studied we could only detect the low frequency relaxation of water.

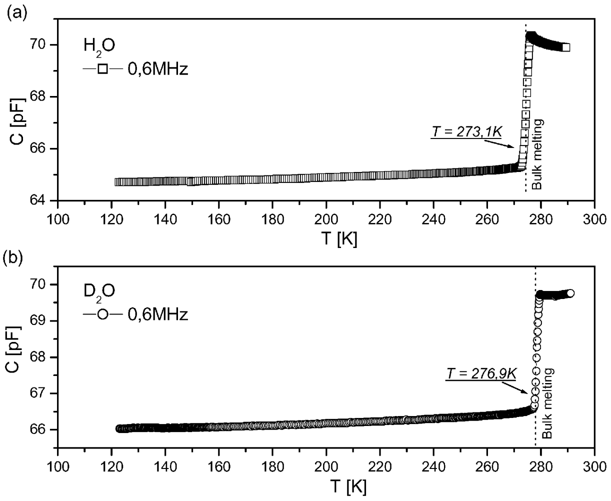

Fig. 1 Capacitance C *vs.* temperature for H_2O and D_2O water.

Analysis of the Cole–Cole representation of the complex capacity for solid H_2O and D_2O water has shown that the relaxation observed can be approximated by a symmetric distribution of relaxation times described formally by the Cole–Cole eqn (1). Examples of the experimental results and the fitted curves are given in Fig. 2 and 3 for the D_2O bulk solid phase at 238 and 128 K, respectively. From the plot of κ' and κ'' *vs.* log ω (Fig. 2 and 3), the relaxation time can be calculated as the inverse of the frequency ω corresponding to a saddle point of the κ' plot or a maximum of the κ'' plot. An alternative graphical representation of the Debye dispersion equation is the Cole–Cole diagram in the complex κ^* plane

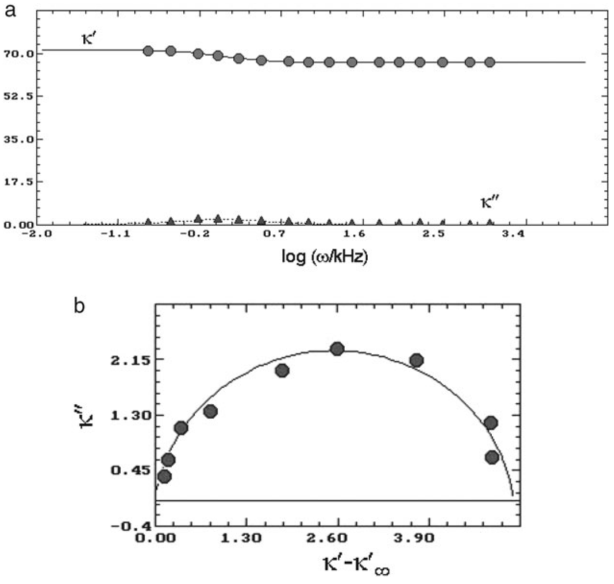

Fig. 2 (a) Spectrum plot for D_2O at 238 K (the solid and the dashed curves are fits to the real and imaginary parts of κ); (b) representation of the spectrum plots in the form of a Cole–Cole diagram for D_2O at 238 K.

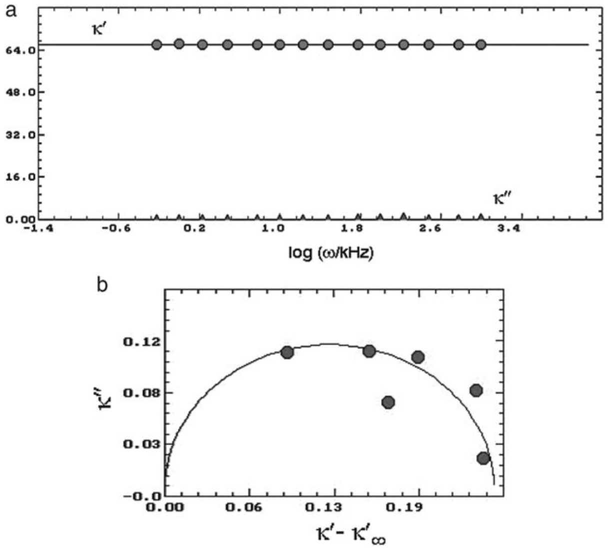

Fig. 3 (a) Spectrum plot for D_2O at 128 K (the solid and the dashed curves are fits to the real and imaginary parts of κ); (b) representation of the spectrum plots in the form of a Cole–Cole diagram for D_2O at 128 K.

(Fig. 2b and 3b). Each relaxation mechanism is reflected as a semicircle in the Cole–Cole diagram. From the plot of κ'' *vs.* κ', the value of τ is given as the inverse of the frequency at which κ'' goes through a maximum. Fig. 4 presents the variation of the relaxation time with temperature for bulk H_2O and D_2O water obtained from fitting eqn (1) to the dispersion spectrum. In the solid phase of H_2O and D_2O (below 273.1 and 276.9 K, respectively), our measurements showed the ordinary ice to have a single relaxation time of the order of 10^{-5}–10^{-3} s in the temperature range from 273 to about 180 K for H_2O, and 193 K for D_2O. This result is consistent with other results,[15,22] and typical of the hexagonal form of ice.[22] At temperatures of about 190 K for D_2O, and 170 K for H_2O, a drastic change in the value of the relaxation time is observed, suggesting a transition to a form of ice that is different from hexagonal. It is known from the ice phase diagram that a transition from the metastable cubic Ic form of ice to hexagonal Ih ice is observed in the temperature range 170–200 K at ambient pressure. Cubic ice crystals convert irreversibly, but very slowly, to hexagonal ice, with up to 50 J mol^{-1} heat evolutions. In contrast to Ih ice, water molecules in Ic ice have a staggered arrangements of hydrogen bonding with respect to *all* of their neighbors, rather than with 3/4 of them as for Ih ice. The result is that the density for Ic ice is almost the same as for Ih ice. The packing efficiency of the cubic ice is about 1/2, while the Ih ice possesses a fairly open low-density structure with a packing efficiency of about 1/3. We can conclude that the much faster relaxation process observed for H_2O and D_2O ice at temperatures below 170–190 K (Fig. 4) describes the relaxation of the cubic form of H_2O and D_2O.

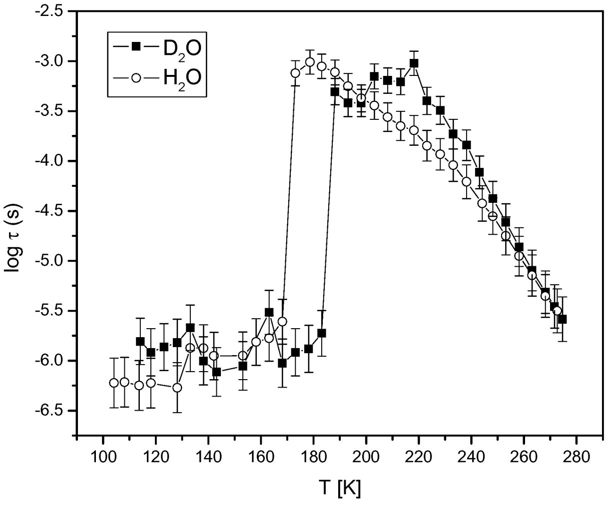

Fig. 4 Dielectric relaxation time τ *vs.* for bulk D_2O and H_2O water.

In Fig. 5 the capacity C is presented as a function of temperature for D_2O water confined in MWNTs, for diameters of 2.4 and 3.9 nm. For comparison, we also show the results for the pore melting temperature for H_2O water in MWNTs of diameter 3.9 nm. Since the samples studied are a suspension of water-filled carbon nanotubes in pure water, the signals contain contributions of both bulk and confined water. In Fig. 5a the feature observed at $T = 276.9$ K in the capacity C *vs.* temperature plot was found at the same temperature for D_2O water adsorbed on pristine MWNTs. Since the latter are essentially closed, this discontinuity is associated with the melting point of bulk D_2O water. By contrast, the sharp increase at $T = 271.6$ K in Fig. 5a is attributed to melting in the pores. The shift of the melting temperature of D_2O water in the MWNTs relative to the bulk is: $\Delta T = T_{\text{bulk}} - T_{\text{MWNT}} = 5.3$ K. In Fig. 5c the function $C(T)$ for H_2O water in MWNTs of diameter 3.9 nm is presented. The pore melting point is attributed to a sharp increase of the $C(T)$ function at 269 K. The depression of the pore melting point relative to the bulk is $\Delta T = 4.1$ K. For D_2O water in MWNTs of diameter 3.9 nm (Fig. 5b) $\Delta T = 4.4$ K, so the depression of the melting point for pores of the same diameter is similar for H_2O and D_2O. The $C(T)$ function for H_2O in MWNTs of diameter 10 nm presented in Fig. 5d shows only one transition point, observed as a discontinuity of $C(T)$ at 273 K, related with the bulk melting point. It suggests that the melting temperature in the pores is almost the same as the bulk melting point, and that the water in carbon nanotubes of 10 nm diameter has a similar molecular arrangement to that of the bulk liquid. Fig. 5e presents the function $C(T)$ for empty carbon nanotubes. The linear temperature dependence of C over the whole temperature range confirms that the effects observed in Fig. 5a–d result from the liquid in the pores.

Similar results were obtained using the DSC method. The melting temperatures were determined from the position of the peaks of the heat flow signals on heating and were reproducible to within 0.5 K. An example of such a DSC scan, corresponding to the melting of D_2O water in MWNTs of diameter 2.4 nm is presented in Fig. 6a. The large endothermic peak at 276.9 K corresponds to the melting of the bulk D_2O water, so the pores are fully filled. In addition, a second peak at 271.4 K is observed, which can correspond to the melting of D_2O water in MWNTs; the melting temperature of D_2O adsorbed in MWNTs is shifted towards lower temperatures

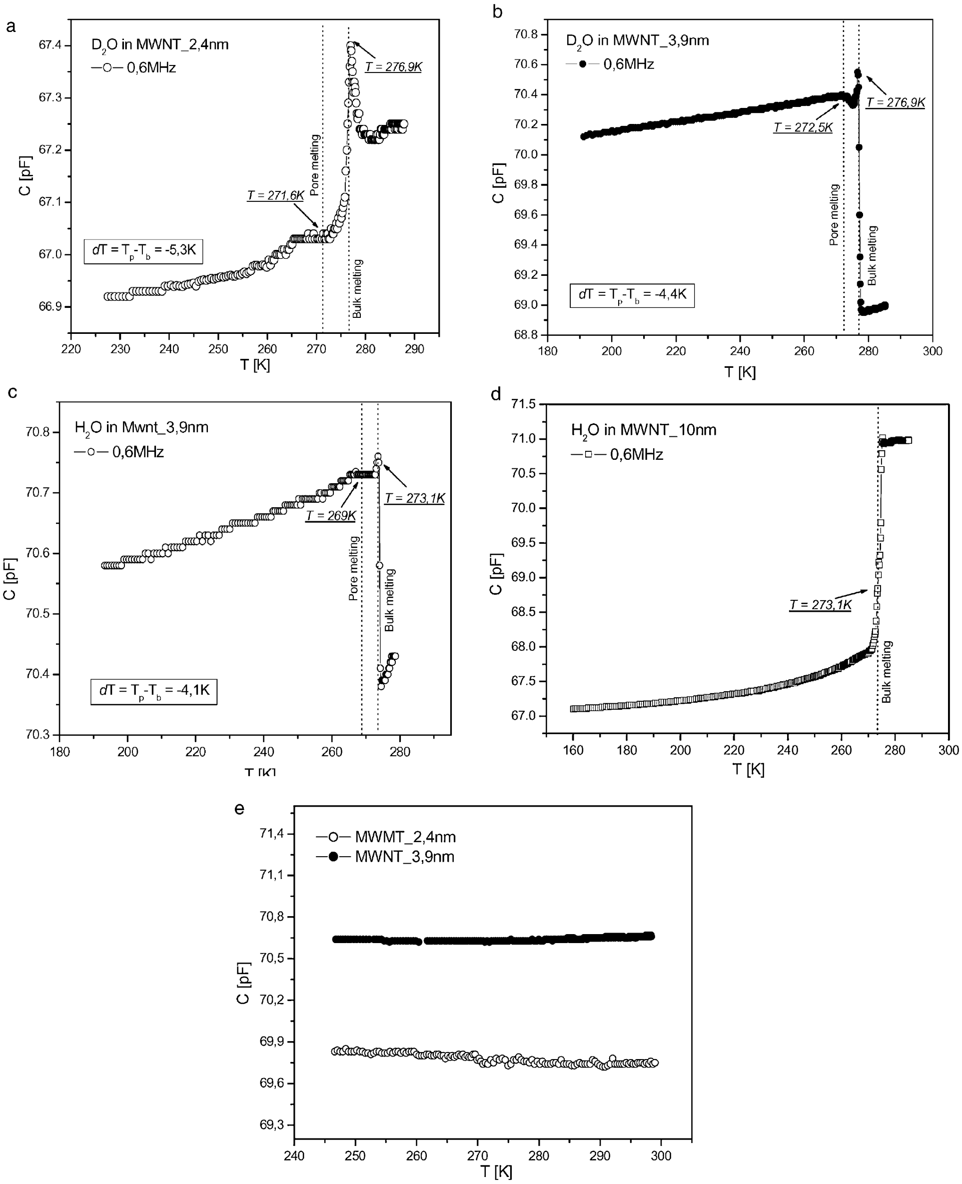

Fig. 5 Capacitance C *vs.* temperature for: (a) D_2O water placed in a MWCN of diameter 2.4 nm, (b) D_2O water in a MWCN of diameter 3.9 nm, (c) H_2O water placed in a MWCN of 3.9 nm, (d) H_2O water in a MWCN of 10 nm diameter, (e) empty MWCNs of diameters 2.4 and 3.9 nm.

by about 5.4 K relative to that of the bulk D_2O water. In Fig. 6b DSC scans for H_2O and D_2O water in MWNTs of 3.9 nm diameter are presented. The large peaks correspond to the melting of the bulk H_2O and D_2O, and second peaks at temperatures of 269.1 and 272.1 K indicate the melting points in pores of H_2O and D_2O water, respectively. The shift of the melting temperature, ΔT, for H_2O is $\Delta T = 4$ K, and for D_2O is $\Delta T = 4.4$ K, and is about 1.4 K lower than for water in MWNTs of 2.4 nm diameter. For water in MWNTs of 10 nm diameter we do not observe a separate and distinct pore melting point (Fig. 6c).

Analysis of the Cole–Cole representation of the complex capacity for H_2O and D_2O water in MWNTs of 3.9 nm diameter at various temperatures is shown in Fig. 7. On the base of the results given above, it can be assumed that ice confined in MWNTs of 3.9 nm diameter melts at 268.4 and 272.1 K for H_2O and D_2O water, respectively; in the temperature range 269.1–273 K (for H_2O), and 272.1–276.9 K (for D_2O), water should be present in the bulk crystal phase and also as liquid in the pores. Fig. 7–9 present the spectrum plot (κ', κ'' *vs.* ω) for D_2O water confined in MWNTs of 3.9 nm of diameter at three different temperatures. The spectrum in Fig. 7a for 274 K represents two relaxation mechanisms, as indicated by the two inflection points in κ'', characterized by relaxation times of the order of 10^{-2} s and 10^{-5} s. The corresponding Cole–Cole diagram is shown in Fig. 7b. In the presence of dipolar constituents, one or more absorption regions are present, not all of them necessarily associated with the dipolar dispersion. At the lowest frequencies (especially about 1 KHz), a large κ'' value arises from the conductivity of the medium, and interfacial (Maxwell–Wagner) polarization is found if the system is not in a single homogeneous phase. For

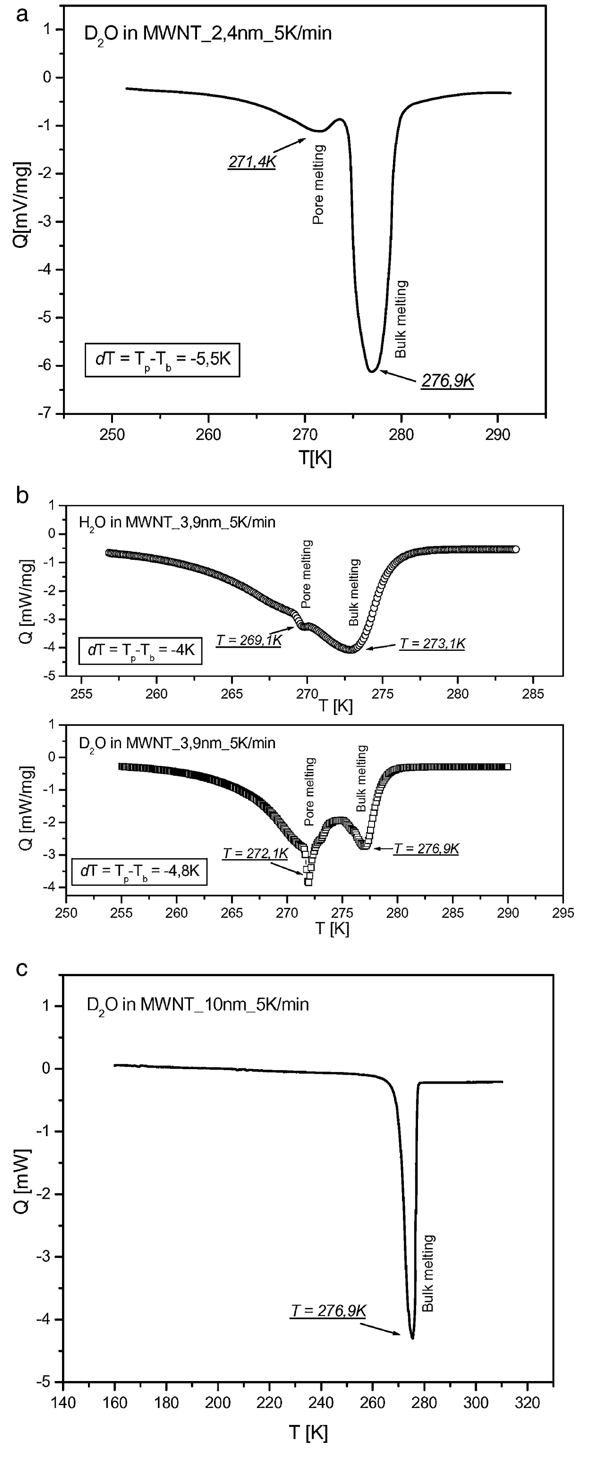

Fig. 6 DSC scans for (a) D_2O water in MWCNs of 2.4 nm of diameter, (b) D_2O and H_2O water in MWCNs of 3.9 nm diameter, (c) D_2O water in MWCNs of 10 nm diameter.

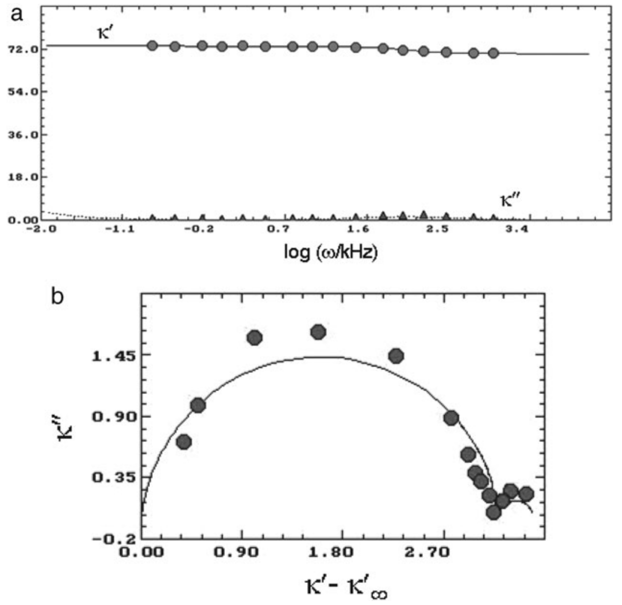

Fig. 7 (a) Spectrum plot for D_2O in MWCNs of diameter 3.9 nm at 274 K (the solid and the dashed curves are fits to the real and imaginary parts of κ); (b) representation of the spectrum plots in the form of a Cole–Cole diagram.

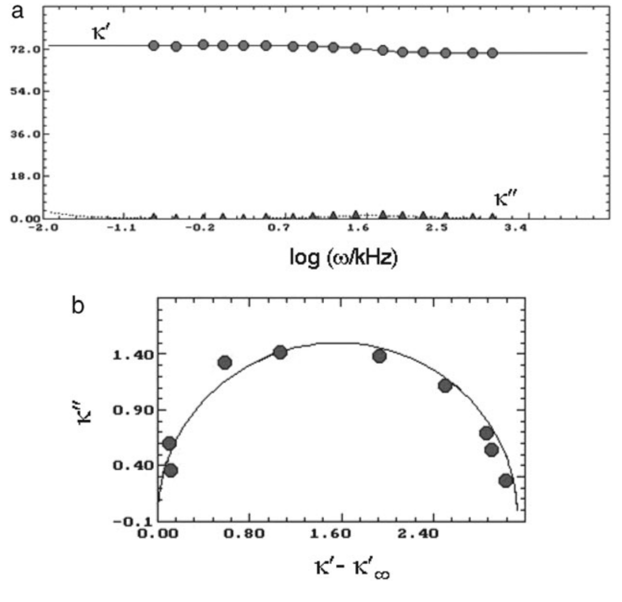

Fig. 8 (a) Spectrum plot for D_2O in MWCNs of diameter 3.9 nm at 258 K (the solid and the dashed curves are fits to the real and imaginary parts of κ); (b) representation of the spectrum plots in the form of a Cole–Cole diagram.

water, a homogeneous medium whose conductivity is of the order of $10^{-6}\ \Omega^{-1}\ \mathrm{m}^{-1}$, the absorption region observed for the frequency 1 KHz is related to the conductivity of the medium. The Joule heat arising from the conductivity contributes to a loss factor $\kappa_{\mathrm{conductance}}''$, so that the value at low frequency is: $\kappa_{\mathrm{total}}'' = \kappa_{\mathrm{dielectric}}'' + \kappa_{\mathrm{conductance}}''$, and the system reveals the energy loss in processes other than dielectric relaxation.[15] In Fig. 7b the component of the relaxation time of the order of 10^{-2} s. characterizes the process of absorption related to the conductivity of the medium. This branch is characteristic of the liquid phase and is a good indicator of the appearance of that phase. The second relaxation mechanism corresponds to a semi-circle in the Cole–Cole diagram in Fig. 7b, characterized by a relaxation time of the order of 10^{-4} s, and is typical of hexagonal ice at this temperature. The spectrum in Fig. 8b for 258 K shows one relaxation mechanism with a relaxation time

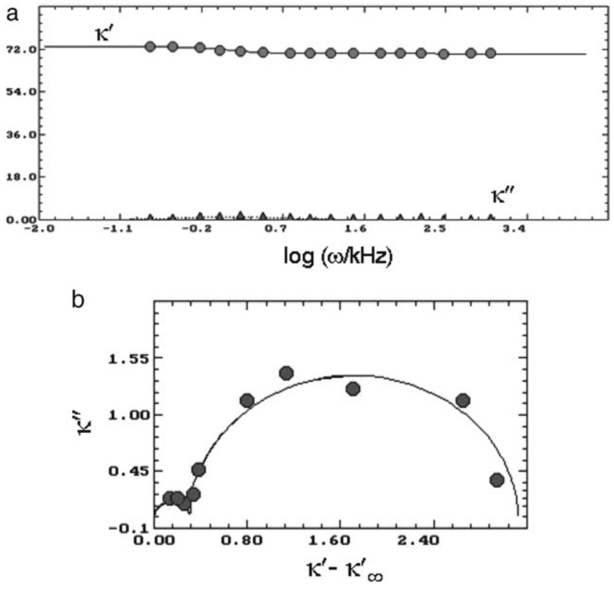

Fig. 9 (a) Spectrum plot for D_2O in MWCNs of diameter 3.9 nm at 200 K (the solid and the dashed curves are fits to the real and imaginary parts of κ); (b) representation of the spectrum plots in the form of a Cole–Cole diagram.

of the order of 10^{-4} s, typical of Ih ice. The spectrum for 200 K, presented at Fig. 9, shows two relaxation mechanisms, corresponding to the two semi-circles in the Cole–Cole diagram, and characterized by relaxation times of the order of 10^{-5} s, typical of Ih at this temperature, and 10^{-6} s, characteristic of the Ic.

The behavior of the relaxation times as a function of temperature for D_2O in MWCN is depicted in Fig. 10. For temperatures higher than 272.1 K (melting point inside the pores) there are two different kinds of relaxation. The larger component of the relaxation time of order 10^{-2} s is strongly dependent on temperature. It is related to the conductivity of water in the pores, and testifies to the presence of the liquid phase in the system. The shorter component of the relaxation time is of the order of 10^{-5} s, and is characteristic of the solid state of bulk water (Ih) for this temperature range. Below the pore melting point, in the range 272.1–245 K, only a branch of shorter relaxation times is observed, characteristic of Debye-type dispersion in Ih; the crystal phase of water occurs in both the pores and in the bulk D_2O water. The results obtained show that the ice melting point in the MWNT pores is 272 K, which is 4.2 K lower than in the bulk. The relaxation times determined indicate the presence of only solid (Ih or Ic crystal form; in this temperature region the relaxation times of Ih and Ic ice are comparable, and are of the order of 10^{-6} s) or liquid micro-phases in the pores. In the temperature range below 240 K an additional branch of the relaxation time, of the order of 10^{-6} s (Fig. 10), is observed; this is a typical relaxation time of the cubic form of ice. Because at higher temperatures the relaxation times of Ih and Ic are similar, it is difficult to distinguish the existence of the two forms of ice at temperatures close to pore melting point. The results in Fig. 10 suggest that for D_2O water confined in MWNT pores a transition from Ic to Ih ice can be observed at a temperature somewhat above 240 K, whereas for bulk phase D_2O water this transition occurs at about 195 K. Thus, the melting transition of D_2O in MWNTs is from Ih ice to liquid, rather than from cubic ice to liquid. Similar conclusions are drawn from an analysis of the behavior of the relaxation times as a function of temperature for H_2O in MWNTs of 3.9 nm diameter, where a similar distribution of relaxation times is observed (Fig. 11). For D_2O water confined in MWNTs of diameter 2.4 nm, the behavior of the relaxation times as a function of temperature is presented at Fig. 12. The distribution of relaxation times has a similar character to that shown in Fig. 10 and 11, but the pore transition temperatures are shifted towards lower temperatures: from cubic to hexagonal ice at a temperature below 240 K, and from hexagonal ice to liquid at 271.6 K.

Neutron diffraction results: water in MWNTs

In order to characterize the structure of water confined in MWNTs we performed neutron diffraction studies for D_2O

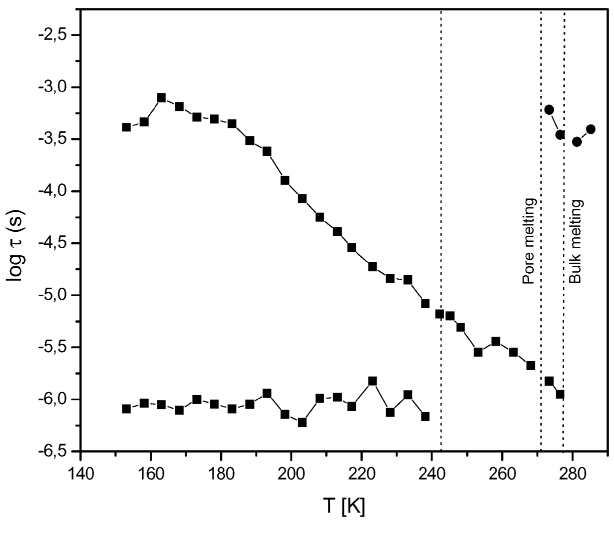

Fig. 10 Dielectric relaxation time τ *vs.* T for D_2O in MWCNs of diameter 3.9 nm.

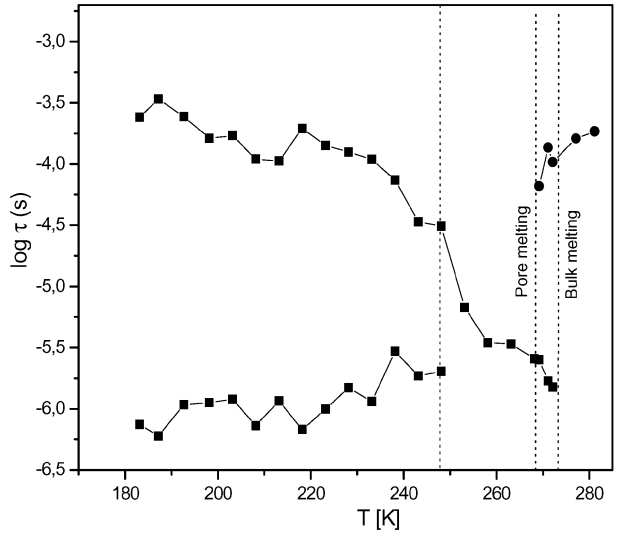

Fig. 11 Dielectric relaxation time τ *vs.* T for H_2O in MWCNs of diameter 3.9 nm.

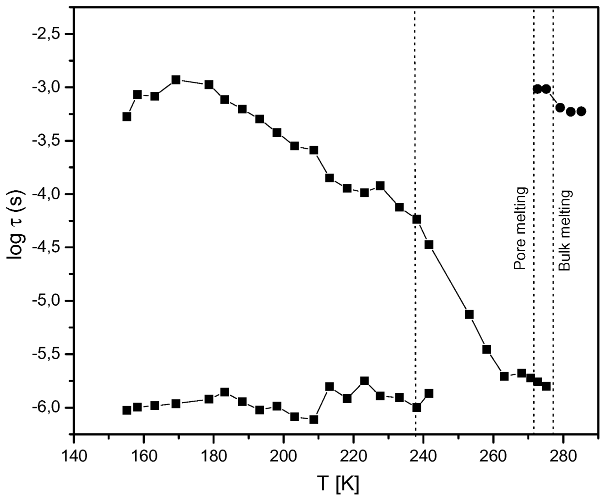

Fig. 12 Dielectric relaxation time τ *vs.* T for D_2O in MWCNs of diameter 2.4 nm.

water in nanotubes of diameters 2.4 and 3.9 nm. The neutron diffraction pattern and the Rietveld refinement for the MWNT powder samples are shown in Fig. 13 for a pore diameter of 2.4 nm at 20 and 290 K. The graphite 3D crystal has a hexagonal structure (space group *P*63/*mmc*). Neutron diffraction revealed the (110), (101) and (102) reflections of the hexagonal lattice of the dry MWNT. In common with most purified carbon nanotube materials, our MWNT samples contain impurities such as Co and Ni nanoparticles up to about 3 wt% in total, and the nanotubes exhibit local defects (holes, cross-links). The local defects and varying microstructure do not affect the interpretation of the neutron data regarding the encapsulated D_2O water, because the low impurity concentration and much larger length scale of the microstructure defects compared to the D_2O water molecules only lead to a negligible and featureless background in the neutron intensity. As follows from Fig. 13, this background is stable over the whole temperature range considered, as the neutron diffraction pattern for dry MWNT is similar at the different temperatures studied. Fig. 14 presents the neutron diffraction spectra at temperatures 280, 276 and 220 K, recorded on a heating cycle for D_2O water encapsulated in MWNTs of diameter 2.4 nm after Rietveld refinements. At 276 K, slightly lower than the bulk D_2O water melting point but higher than the pore melting temperature, the neutron diffraction spectrum is typical of hexagonal ice (Ih) with the space group *P*63/*mmc*. The characteristic triplet of hexagonal ice is clearly visible at 3.44, 3.66, 3.89 Å, with additional single peaks at the positions: 1.47, 1.72, 2.25, 2.67 Å. At lower temperature (220 K), below the pore melting point, there is a broader peak structure characteristic of cubic ice, with the space group *Fd*3̄*m*, where additional peaks at the positions: 1.04, 1.46, 1.83, 1.91, 3.67 Å are observed. At 280 K, D_2O bulk and D_2O inside the pores are in the liquid phase and in the neutron diffraction spectrum only the peaks from dry MWCN are visible (Fig. 14a). The changes in the diffraction pattern as a function of temperature in the region of the main peaks are shown in Fig. 15. The sequence illustrates the difference between the composite phase, where the hexagonal ice has formed outside the pores but the liquid phase is still in the pores (Fig. 15c and e), and the phase showing the characteristic triplet shape of cubic ice at 3.65–3.69 Å (Fig. 15b and d). The hexagonal ice peaks are sharp, indicating a large crystallite size, and the peak positions show a systematic displacement with temperature. The results of Rietveld refinement for the diffraction pattern of Ih and Ic ice presented in Fig. 15a show that the spectrum obtained at 220 K is a superposition of the Ih and Ic spectra. In Fig. 15c the neutron spectrum for D_2O confined at MWNTs of 3.9 nm diameter is presented. It also shows the existence of cubic ice at temperatures below the pore melting point.

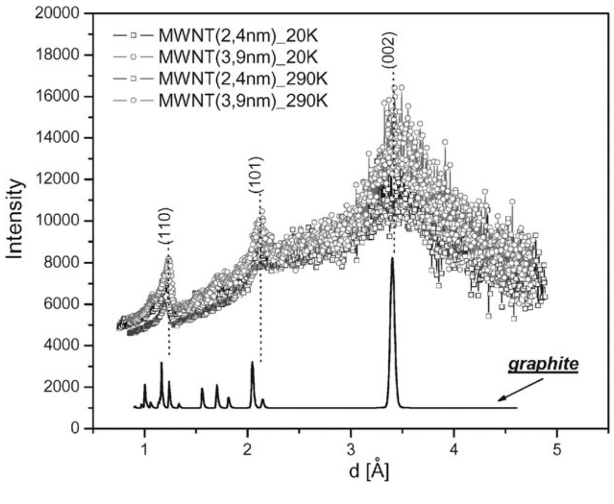

Fig. 13 Neutron diffraction pattern and the results of Rietveld refinement of empty MWCNs of 2.4 and 3.9 nm diameters at temperatures of 20 and 290 K.

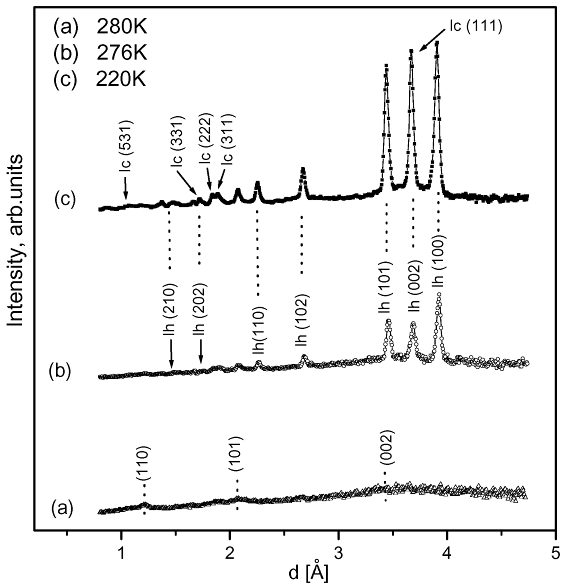

Fig. 14 Neutron diffraction spectra for D_2O in MWCNs of 2.4 nm diameter at temperatures of: (a) 280 K, (b) 276 K and (c) 220 K.

The formation of cubic ice in confined water has been observed previously for water confined in silica mesopores,[23–28] but not for water in carbon nanotubes. Suppression of the crystal growth of ice in cylindrical mesopores can be an important factor for the formation and stability of cubic ice.

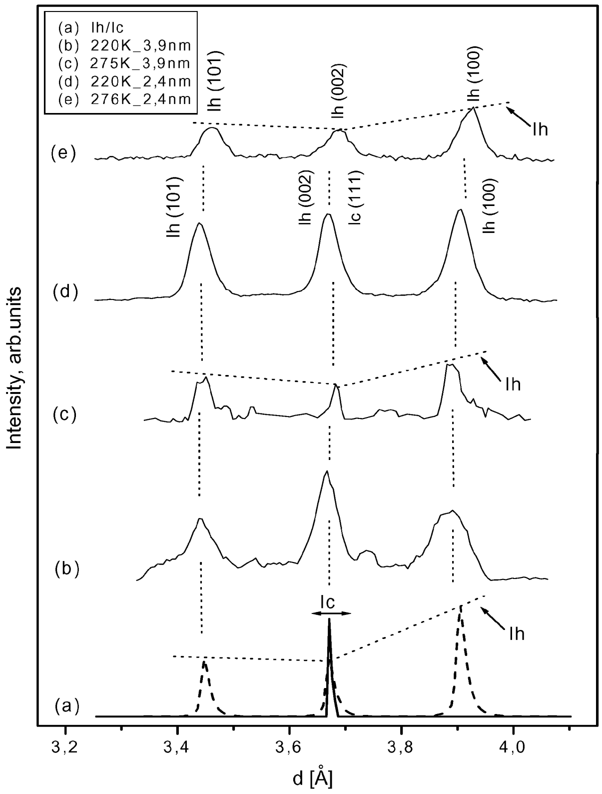

Fig. 15 The variation of the profile of the main diffraction peaks and the Rietveld refinement (a) for D_2O water in: (b) water in MWCNs of 3.9 nm diameter at 220 K, (c) water in MWCNs of 3.9 nm diameter at 275 K, (d) water in MWCNs of 2.4 nm diameter at 220 K, (d) water in MWCNs of 2.4 nm diameter at 220 K.

The results presented in this paper serve to further define the temperature range over which cubic ice appears in silica mesopores, and show for the first time that cubic ice is also observed for water confined in carbon nanotubes with diameters of 2.4 and 3.9 nm, at temperatures below the pore melting points. Furthermore, we evidenced by comparison of cylindrical carbon and silica pores the essential influence of the pore geometry for the structure of solid state of water.

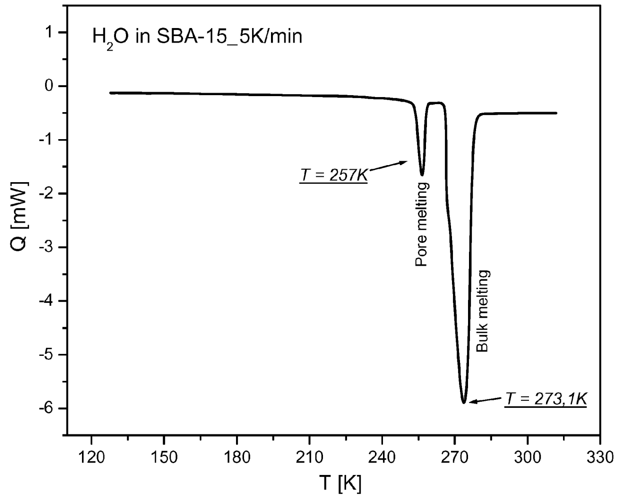

Fig. 16 DSC scans for water in SBA-15 silica pores of diameter 3.8 nm.

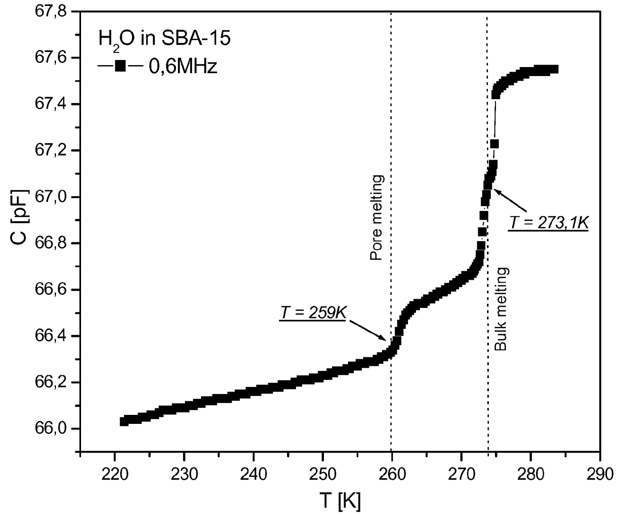

Fig. 17 Capacitance *C vs.* temperature for water in SBA-15 silica pores of diameter 3.8 nm.

Water in silica glass

The melting temperature of H_2O water confined in cylindrical, ordered silica glass SBA-15 having pores of diameter 3.9 nm was determined using DSC and dielectric methods. In Fig. 16 the DSC scan for this sample is presented; the large peak at 273 K corresponds to the melting of the bulk H_2O, and a second peak observed at 257 K corresponds to the melting of H_2O water in the pores of SBA-15. The melting temperature of H_2O adsorbed in the pore of SBA-15 is shifted towards lower temperatures by 16 K relative to that of the bulk H_2O.

The capacitance *C* and tangent loss tan(δ) as a function of frequency and temperature were also measured for water confined in SBA-15. In Fig. 17 the behaviour of *C vs. T* for water in SBA-15 is presented at the frequency of 0.6 MHz The sharp increase at 259 K is attributed to melting in the pores, while that at 273 K corresponds to the bulk melting. The frequency spectrum at a particular temperature is used to obtain the orientational relaxation times in the different phases of the system, as described above. In Fig. 18a and 19a the spectrum plot (κ' and κ'' *vs.* ω) is shown for water in SBA-15 at two different temperatures. The spectrum at 208 K shows two relaxation mechanisms (as seen by two inflection points in κ'') with relaxation times of the order of 10^{-4} s and 10^{-6} s. A similar spectrum at 250 K shows just one relaxation mechanism with a time scale of 10^{-5} s. The corresponding Cole–Cole diagrams are shown in Fig. 18b and 19b. In Fig. 20 the spectrum at 270 K again shows two relaxation mechanisms with relaxation times of the order of 10^{-6} s and 10^{-4} s. The behaviour of the relaxation times as a function of temperature for water in SBA-15 is depicted in Fig. 21. In the temperature range between the bulk and pore melting points (273–267 K) two branches of the relaxation time are observed: the longer component, 10^{-3} s, corresponds to the response of the liquid phase in the pore, and the shorter component corresponds to hexagonal ice in the bulk phase. In the temperature range 220–267 K there is one relaxation time, typical of Ih ice, but

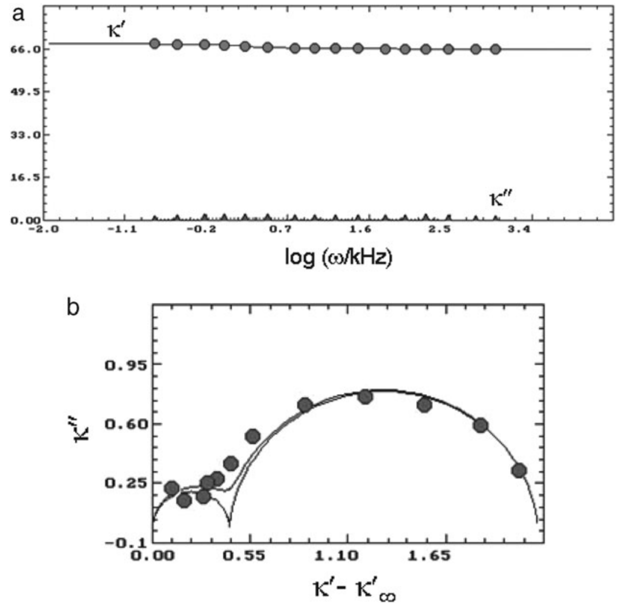

Fig. 18 (a) Spectrum plot for H_2O in SBA-15 having a pore diameter of 3.8 nm at 208 K (the solid and the dashed curves are fits to the real and imaginary part of κ); (b) representation of the spectrum plots in the form of a Cole–Cole diagram.

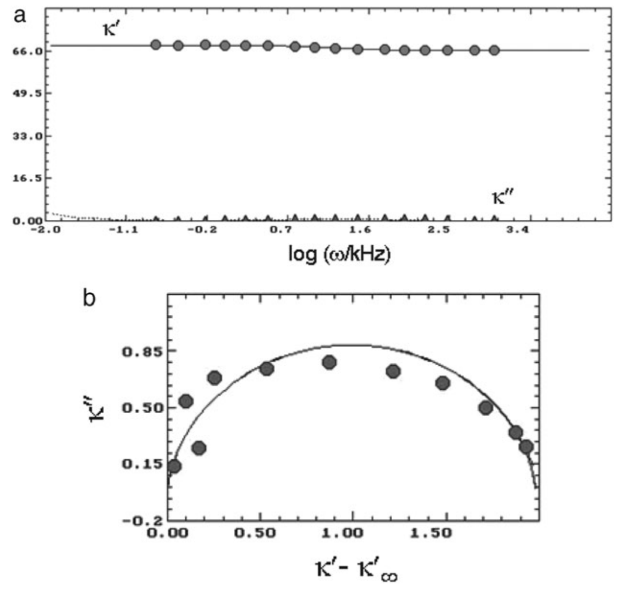

Fig. 19 (a) Spectrum plot for H_2O in SBA-15 having a pore diameter of 3.9 nm at 250 K (the solid and the dashed curves are fits to the real and imaginary parts of κ); (b) representation of the spectrum plots in the form of a Cole–Cole diagram.

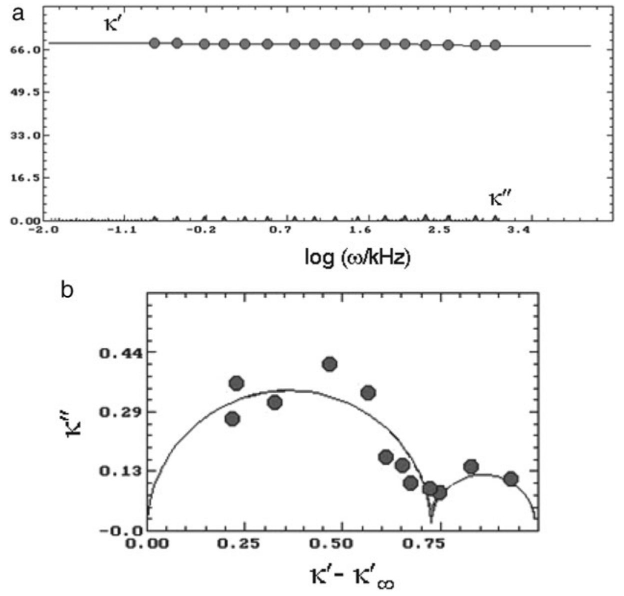

Fig. 20 (a) Spectrum plot for H_2O in SBA-15 having a pore diameter of 3.9 nm at 270 K (the solid and the dashed curves are fits to the real and imaginary parts of κ); (b) representation of the spectrum plots in the form of a Cole–Cole diagram.

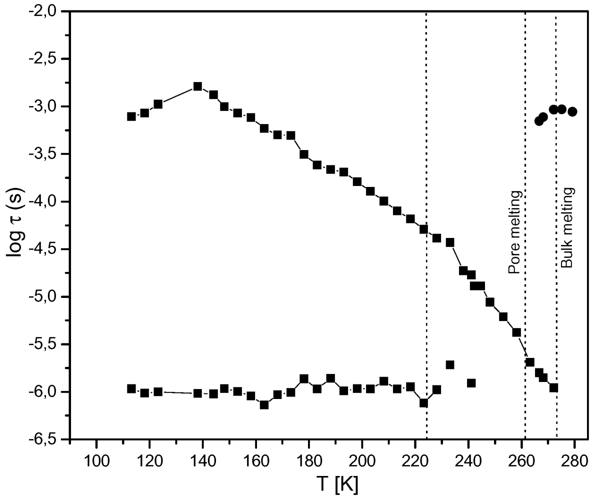

Fig. 21 Dielectric relaxation time τ *vs.* temperature for water in SBA-15.

close to the pore melting point of 267 K it has a value 10^{-6} s, which is also typical of cubic ice. In the temperature range 100–220 K two stable components of the relaxation times, characteristic of Ih and Ic ice, are observed. This result suggests that for water confined in cylindrical SBA-15 pores, stable cubic ice exists in the pores at lower temperatures. The existence of cubic ice in SBA-15 was reported from neutron and X-ray diffraction experiments performed for water in MCM and SBA silica mesopores.[23–28] It was shown that the cubic form of ice is stable in SBA-15 pores at temperatures below 220 K, and that the melting point of the defective cubic ice in pores is depressed below the bulk melting point. We obtained similar results also for water confined in Vycor Glass by analysis of dielectric behaviour of this system.[28]

Discussion and results

We have observed depression of the freezing point for water confined in the cylindrical pores of both carbon nanotubes and mesoporous silica, with the depression being much greater for SBA-15 than for the MWNT's of similar pore diameter. We also observe the formation of cubic ice in both materials at temperatures below the pore freezing temperature. The similar

Table 1 Parameters for systems studied[a]

	Carbon nanotube	Silica	H_2O
σ/nm	0.34	0.27	0.32
ε, k_B/K	28.0	230.0	401.0
ρ_w/nm^{-3}	114	57.2	
Δ/nm	0.33	0.22	

[a] The ρ_w (density of surface oxygen atoms per unit area) for silica is calculated with the help of Material Studio software (Visualizer (Materials Studio 2.0), Accelrys Inc., San Diego, CA, 2001.) Other parameters come from the literature.[16,30] The Lorentz–Berthelot mixing rules were used to calculate the cross parameters σ_{fw} and ε_{fw}. For H_2O–carbon nanotubes: $\sigma_{fw} = 0.33$ nm, $\varepsilon_{fw}/k_B = 106.0$ K; while for H_2O–silica: $\sigma_{fw} = 0.295$ nm, $\varepsilon_{fw}/k_B = 303.7$ K.

behaviour of the two materials in the formation of cubic ice, despite significant differences in the fluid-wall interaction energies for silica SBA-15 and carbon MWNTs (see below), suggests that cubic ice formation is a result of entropic effects due to strong confinement by the cylindrical pore walls, regardless of the porous material. We note that cubic ice has a more packed structure (coordination number 12) than hexagonal ice (coordination number 8). Our results seem to be consistent with recent H^1 and H^2 NMR studies by Matsuda *et al.*[12] on water in SWNT's with an average diameter of 1.3 nm, which showed tube-like ice structures with a long-range order for temperatures below 220 K.

The differences in melting point depression for silica and carbon mesopores are consistent with the results of molecular simulations,[2,16] as we now discuss. The influence of energetics (fluid–fluid and fluid-wall interactions) on the freezing/melting behavior of the fluids of small molecules confined in porous materials can be understood in terms of two main parameters, as proposed in our previous work.[16] One is the pore width H^* which is expressed as a multiple of the diameter of the fluid molecule. The other is the parameter α, which is the ratio of the fluid–wall to the fluid–fluid attractive interaction, $\alpha = \frac{\rho_w \varepsilon_{fw} \sigma_{fw}^2 \Delta}{\varepsilon_{ff}}$, where Δ is the inter-layer spacing in the solid and ρ_w is the number of wall atoms per unit area. Thus the value of α depends not only on the ratio of the two well depths, but also depends strongly on the density of wall atoms, the interlayer spacing, and the fluid–wall diameter parameter, σ_{fw}. This density is 114 nm^{-2} for carbon, but only half as much, 57 nm^{-2} for silica. In addition, both σ_{fw} and Δ are considerably smaller for silica than for carbon (see Table 1). While it is true that the fluid–wall energy well depth is larger for silica than for carbon, this effect is more than compensated for by these differences in surface density, σ_{fw} and Δ, so that the values of α are 1.08 for water–carbon, and only 0.83 for water–silica. Our previous results,[16] supported by other literature [*e.g.* ref. 29], indicate that the threshold α value for Lennard-Jones fluids in smooth walled pores is 1.15; thus for $\alpha > 1.15$ we expect (based on numerous simulation results for slit-shaped pores) an elevation in freezing temperature, and a depression in freezing temperature is expected for $\alpha < 1.15$. Thus, based on energetic considerations alone, we expect a decrease in the freezing temperature for both carbon and silica pores, with a more pronounced decrease in the case of the silica pores. This is what is observed in our experimental results. We note that the magnitude of the shift in freezing temperature appears to be strongly dependent on the pore geometry.

While the direction of the shift in the freezing temperature depends on the value of α, its *magnitude* seems to depend strongly on pore geometry and pore disorder (surface roughness, tortuosity, connectivity—see ref. 31), and in general seems to be considerably larger for disordered slit shaped pores (as in activated carbon fibers) than for cylinders. Thus for carbon tetrachloride in carbons, with $\alpha \sim 1.92$,[16] for ACF an upwards shift in freezing temperature of about 60 and 90 K was observed in experiment (DSC) and molecular simulation, respectively,[32] whereas carbon tetrachloride in multi-walled carbon nanotubes shows an upward shift in freezing temperature of only 6 or 7 K.[30] The same appears to be the case here for water, in that the magnitude of the shift (now a lowering of freezing temperature) is much smaller for the nanotubes than for ACF. It is not yet clear to what extent this large effect is due to differences in the pore geometry or to the pore disorder; it is presumably an entropic effect, and warrants further investigation.

Some previous experimental studies have found evidence of a contact layer phase in silica mesopores, in which the crystalline phase within the pore is separated from the pore walls by a thin layer of liquid water, 1 to 3 molecules thick. Our experimental results do not confirm or deny this; it may well be present but the signal due to the very thin liquid layer may be too weak to detect. Molecular simulations[16] predict such a contact layer phase for water in silica mesopores, with $\alpha = 0.83$, for this size range, but probably not for water in carbon nanotubes, with $\alpha = 1.08$.

Acknowledgements

We thank Dr A. Beskrowny of the Joint Institute for Nuclear Research, Dubna, Russia for fruitful discussions and assistance with the neutron experiments. We also thank the Polish Ministry of Science and Higher Education (MNiSW) for support under GranNo. NN202070333, and the US Department of Energy (GranNo. DE-FG0298ER14847) for partial support of this work.

References

1. L. D. Gelb, K. E. Gubbins, R. Radhakrishnan and M. Sliwinska-Bartkowiak, *Rep. Progr. Phys.*, 1999, **62**, 1573.
2. C. Alba-Simionesco, B. Coasne, G. Dosseh, G. Dudziak, K. E. Gubbins, R. Radhakrishnan and M. Śliwinska-Bartkowiak, *J. Phys.: Condens. Matter*, 2006, **18**, R15.
3. D. Takaiwa, K. Koga and H. Tanaka, *Mol. Simul.*, 2007, **33**, 127.
4. K. Koga and H. Tanaka, *J. Chem. Phys.*, 2006, **124**, 131103.
5. K. Koga, G. T. Gao, H. Tanaka and X. C. Zeng, *Nature*, 2002, **412**, 802.
6. A. Striolo, A. A. Chialvo, K. E. Gubbins and P. T. Cummings, *J. Chem. Phys.*, **122**, 234712.
7. A. I. Kolesnikov, J. M. Zanotti, C. K. Loong, P. Thiyagarajan, A. P. Moravsky, R. O. Loufty and C. J. Burnham, *Phys. Rev. Lett.*, 1999, **93**, 035503.
8. G. Hummer, J. C. Rasaiah and J. P. Noworyta, *Nature*, 2001, **414**, 188.
9. H. Tanaka and K. Koga, *J. Chem. Phys.*, 2005, **123**, 094706.
10. J. Zheng, E. M. Lemmon, H. A. Tsao, H. J. Sheng and S. Jiag, *J. Chem. Phys.*, 2005, **122**, 214702.

11. J. C. Dore, J. W. B. Webber and J. H. Strange, *Colloid Surf. Sci. A*, 2004, **241**, 191.
12. K. Matsuda, T. Hibi, H. Kadouaki, H. Kataura and Y. Maniwa, *Phys. Rev. B: Condens. Matter Mater. Phys.*, 2006, **74**, 073415.
13. M. Sliwinska-Bartkowiak, G. Dudziak, R. Sikorski, R. Gras, R. Radhakrishnan and K. E. Gubbins, *J. Chem. Phys.*, 2001, **114**, 950.
14. M. Sliwinska-Bartkowiak, G. Dudziak, R. Sikorski, R. Radhakrishnan, L. Gelb and K. E. Gubbins, *Langmuir*, 1999, **15**, 6060.
15. M. Sliwinska-Bartkowiak, G. Dudziak, R. Sikorski, R. Gras, K. E. Gubbins and R. Radhakrishnan, *Phys. Chem. Chem. Phys.*, 2001, **3**, 1179.
16. R. Radhakrishnan, K. E. Gubbins and M. Sliwinska-Bartkowiak, *J. Chem. Phys.*, 2000, **112**, 11048; R. Radhakrishnan, K. E. Gubbins and M. Sliwinska-Bartkowiak, *J. Chem. Phys.*, 2002, **116**, 1147.
17. A. Chełkowski, *Dielectric Physics*, Elsevier, North-Holland, 1990.
18. B. Szurkowski, T. Hilczer and M. Sliwinska-Bartkowiak, *Ber. Bunsen-Ges. Phys. Chem.*, 1993, **97**, 731.
19. H. M. Rietveld, *J. Appl. Crystallogr.*, 1969, **2**, 65.
20. V. B. Zlokazov and V. V. Chernyshev, *J. Appl. Crystallogr.*, 1992, **25**, 447.
21. A. Beskrovny, N. Guskos, J. Typek, N. Ryabova, A. Blonska-Tabero and G. Zołnierkiewicz, *Rev. Adv. Mater. Sci.*, 2006, **12**, 166.
22. N. Hill, W. E. Vaughan, A. H. Price and M. Davies, in *Dielectric Properties and Molecular Behaviour*, ed. T. M. Sugden, Van Nostrand, Reinhold, New York, 1970.
23. J. Dore, B. Webber, M. Hartl, P. Behrens and T. Hansen, *Physica A*, 2002, **314**, 501.
24. B. Webber and J. Dore, *J. Phys.: Condens. Matter*, 2004, **16**, S5449.
25. J. M. Baker, J. Dore and P. Behrens, *J. Phys. Chem. B*, 1997, **101**, 6226.
26. K. Morishige and H. Uematsu, *J. Chem. Phys.*, 2005, **122**, 044711.
27. K. Morishige and H. Iwasaki, *Langmuir*, 2003, **19**, 2808.
28. M. Sliwinska-Bartkowiak and M. Jazdzewska, to be published.
29. K. G. Ayappa and R. K. Mishra, *J. Phys. Chem. B*, 2007, **111**, 14299.
30. F. R. Hung, B. Coasne, E. E. Santiso, K. E. Gubbins, F. R. Siperstein and M. Sliwinska-Bartkowiak, *J. Chem. Phys.*, 2005, **122**, 144706.
31. B. Coasne, S. K. Jain, L. Naamar and K. E. Gubbins, *Phys. Rev. B: Condens. Matter Mater. Phys.*, 2007, **76**, 085416.
32. R. Radhakrishnan, K. E. Gubbins, A. Watanabe and K. Kaneko, *J. Chem. Phys.*, 1999, **111**, 9058.